npj | Materials Degradation

www.nature.com/npjmatdeg

ARTICLE OPEN

Check for updates

The role of chromium content in the long-term atmospheric corrosion process

Baozhuang Sun[1], Xiaomei Zuo[1], Xuequn Cheng[1,2]✉ and Xiaogang Li[1,2]✉

The corrosion of alloy steels with different amounts of Cr was studied using electrochemical tests, wet–dry cycle corrosion, X-ray diffraction, and Kelvin probe force microscopy. The results show that the content of Cr is positively correlated with the corrosion resistance of bare steel, but the corrosion resistance of atmospheric corrosion does not show the same pattern. The atmospheric corrosion resistance of Cr-containing steel exhibits three different stages with the change of Cr element content. When the Cr content is in the range of 1–4%, the corrosion rate is high and does not change within the Cr content. As the Cr content was further increased from 4 to 7%, the corrosion rate exhibited a linear decrease and then drops rapidly when the Cr content reaches 8%. These three different corrosion rate stages are related to the influence of Cr content on Fe_3O_4 content in the rust layer.

npj Materials Degradation (2020)4:37 ; https://doi.org/10.1038/s41529-020-00142-5

INTRODUCTION

It is well known that the corrosion resistance of materials can be improved by adding corrosion-resistant alloying elements[1–3]. In recent years, a method to improve the corrosion resistance of materials is to form a dense and stable rust layer. One of the typical examples is weathering steel. By adding certain amounts of corrosion-resistant elements, a dense rust layer is formed on the steel surface, which can impede further corrosion process of the substrate to achieve improvement of the steel corrosion resistance[4–8]. The recent researches have suggested that addition of Cr, Cu, or P alloying elements can significantly improve the rust layer structure stability of the weathering steel, thereby improving its applicability in severe industrial and marine environments[9–15].

Several studies have focused on the effect of alloying elements on the corrosion resistance. A study by Ma et al.[16] on the atmospheric corrosion behavior of weathering steel in the tropical marine environment found that the weathering resistance of weathering steel is related to the deposition of chloride ions and the enrichment of Cr in the rust layer and that the latter can significantly improve the corrosion resistance of weathering steels in environments with low chloride ion deposition. Several studies[17–21] found that Cu can enhance the stability of the rust layer when used together with Cr, thus improving the corrosion resistance of weathering steel. However, a minimum of 0.10 wt% Cu is required in order to significantly improve the corrosion resistance of the steel[22]. The rust layer of corrosion-resistant steel after long-term exposure to the atmosphere has a two-layer construction, and a significant difference Cr content presents in the inner and outer layers, respectively[23]. A Cr-enriched inner layer mainly consists of α-$(Fe_{1-x}Cr_x)OOH$, a Cr substituted FeOOH, which acts as a final stable protective layer. Other studies also found that a pseudo-passivation film formed on some Cr-containing steels in the CO_2 corrosion environment, and this film is consisted of $Cr(OH)_3$[24,25]. After analyzing the rust layer structure of Cr-containing steel, Jiang et al.[26] found that Cr is mainly in the forms of $Cr(OH)_3$, CrOOH, or $FeCr_2O_4$ in the rust layer, that is, Cr mainly exists in the form of Cr^{3+} among the participants during the iron oxide process. Yamashita et al.[27] believed that the existence of Cr element can replace the nano-sized goethite particles to create a denser protective rust layer in the inner rust layer. Although all the existing studies so far used several alloying elements together[28,29], it is not difficult to see from these studies that the Cr content and the corrosion resistance have a close correlation. However, the study of the influence of chromium on the initial stages of the atmospheric corrosion of weathering steels by Kamimura and Stratmann[21] found that the positive effect of chromium is not only not apparent in saline environments but also seems to be even harmful by accelerating weathering steels corrosion in coastal environments. Other researchers[30–32] also pointed out that the presence of 0.60–1.30 wt% Cr was sometimes slightly detrimental, especially in industrial atmospheres. Therefore, the effect of the Cr content on the formation of the weather-resistant rust layer in steel, as well as the relationship between the Cr content and the density of the rust layer, has not yet reached a consentient understanding.

In this work, the steel samples with eight different Cr contents were studied to identify the relationship between the Cr content and the atmospheric corrosion resistance. A dry–wet cyclic corrosion test was used to study the effect of the Cr content on the corrosion resistance of the corrosion layer during the atmospheric corrosion process. The purpose of this study is to provide an insight into the influence of the Cr content on atmospheric corrosion resistance. In addition, this study may provide useful data for the development of micro-alloyed corrosion-resistant materials.

RESULTS

Microstructure

The metallographic structure of the eight experimental materials is shown in Fig. 1. It can be seen from the figure that Cr changes the microstructure of the matrix. The Cr content primarily affects the proportion of bainite in the steel. The W1 structure is essentially ferrite with a very small amount of lath bainite. W2, W3, and W4 are both granular bainite and ferrite. As the Cr content increases, the proportion of granular bainite increases gradually.

[1]Corrosion and Protection Centre, University of Science and Technology Beijing, 100083 Beijing, China. [2]Key Laboratory for Corrosion and Protection (MOE), 100083 Beijing, China. ✉email: chengxuequn@ustb.edu.cn; lixiaogang@ustb.edu.cn

This occurs because the addition of Cr to a steel can delay the pearlite transformation and promote the bainite transformation, making it easier to form the bainite structure at a slow cooling rate after austenitizing. When the Cr content reaches ≥5%, the structure is all bainite, and the size of bainite becomes finer with the increase of Cr content; the W8 has the smallest grain size.

Wet–dry cycles corrosion results

To study the atmospheric corrosion behavior of the steels with different Cr contents, dry and wet cycle experiments were carried out on the eight steel samples. Figure 2 shows that, as the corrosion cycles increased, the corrosion rate gradually stabilizes. At the initial stage of the experiment, the main reaction is the

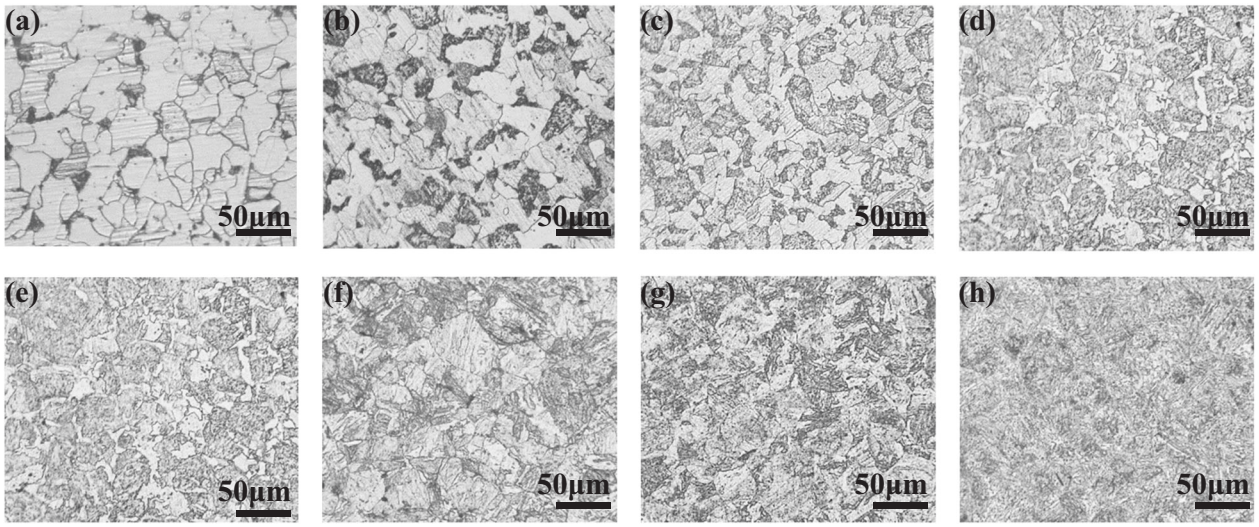

Fig. 1 Metallographic structure of samples with various Cr content. a–h correspond to W1–W8 samples, respectively, and as the Cr content increases, the proportion of granular bainite increases gradually.

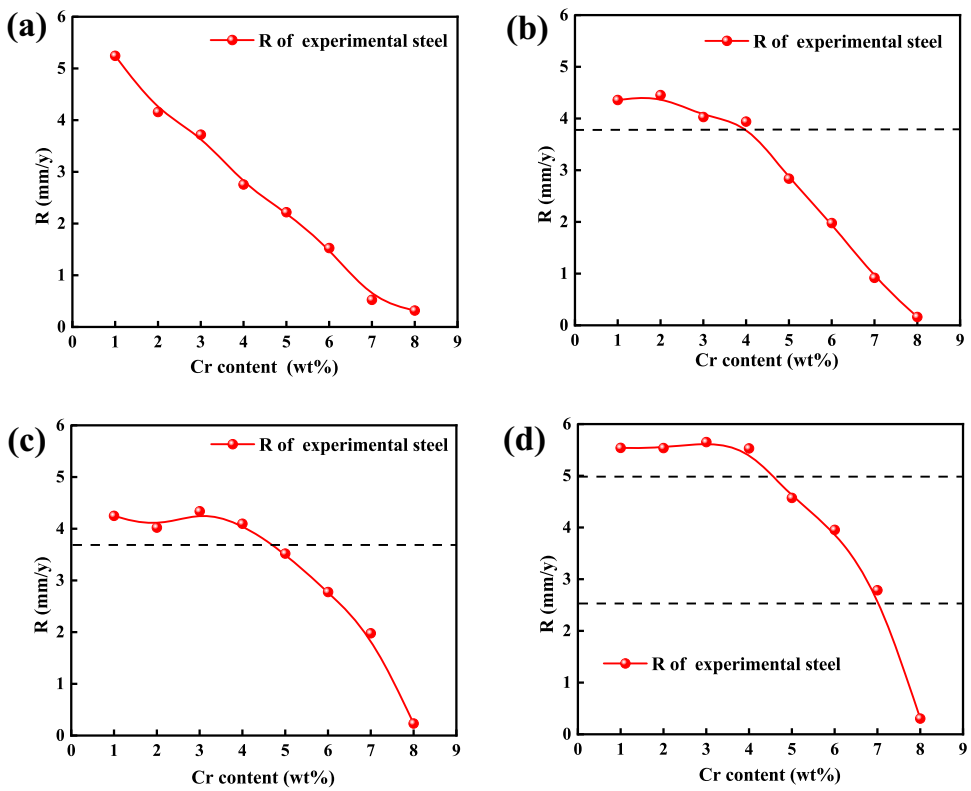

Fig. 2 Corrosion rate of eight experimental steels during alternating wet–dry test in 0.5% NaCl (pH = 3) solution. a 24 h, **b** 72 h, **c** 120 h, **d** 168 h. The dotted line corrosion rate in **b** is 3.8 mm y^{-1}, the dotted line in **c** for 3.7 mm y^{-1}, and the dotted lines in **d** for 5 and 2.5 mm y^{-1}, respectively. Based on corrosion rate variation, there are two corrosion stages in **b**, **c** and three in **d**.

corrosion of the steel substrate. Therefore, the corrosion rate gradually decreases with the increase of Cr content. The Cr content showed a certain positive effect on the corrosion resistance in the early stage of corrosion. However, after the 72-h dry–wet cycle accelerated experiment, the corrosion rate change started to show two different trends for the samples with different Cr contents. The effect of Cr on corrosion rate of the samples with low Cr contents (W1–W4) decreased gradually and trended to be the same, while the effect of Cr on corrosion resistance in those with high Cr content (W5–W8) still showed a positive correlation with the Cr content. This is mainly due to the gradual formation of the rust layer on the steel surface during the prolonged experiment time, where the main factor that affects the corrosion resistance has shifted from the corrosion resistance of the steel substrate to the density of the rust layer. The results after 120-h experiment show no more significant difference in the corrosion rate when the Cr content is the steel is <4%. The result from long-period cycling corrosion test indicated that 4% Cr content appeared to be a threshold for its role in affecting the corrosion rate. After the 168-h dry and wet cycle corrosion experiment (Fig. 2d), a stable rust layer structure has been formed on the surface of the material, and the corrosion rate at this time can be divided into 3 groups: (1) The corrosion rates of W1–W4 are basically the same, at ~5.5 mm y^{-1}. (2) The corrosion resistance of W4–W7 gradually increases, and the corrosion rate decreases linearly from 5.5 to 2.7 mm y^{-1}; (3) The corrosion rate of W8 is only 0.3 mm y^{-1}, which is merely one-eighteenth of W1.

The macroscopic morphology (Supplementary Fig. 1) of the eight experimental materials after wet–dry cycles corrosion test shows that, at 24 h, the surface of the experimental steel features a thin layer of corrosion products, which is relatively flat and does not bubble. The surface rust layers of W1–W6 are predominantly dark brown, with some yellow-brown rust spots; W7 has a small amount of brick red rust on the surface, and W8 exhibits only a very slight corrosion and the substrate is visible. At 72 h, the presence of corrosion products is clearly more noticeable compared with 24-h samples but still not dense. There is obvious surface bubbling for W1–W4. The surface rust layers for W5–W7 are relatively flat. W8 is evenly covered with yellowish brown rust and is very dense. After 120 h, bubbling was observed for W5–W7, and there was no change in the surface appearance for W8. After 168 h, the degree of corrosion had obviously increased, the rust layer morphology for W1–W4 exhibited no difference, the corrosion extent for W5–W7 gradually reduced, and for W8 the surface was still covered in the yellow-brown rust layer, and the corrosion was trivial. Furthermore, the microscopic morphology of corrosion products after 168 h (Supplementary Fig. 2) show that the surfaces of W1–W7 feature more corrosion products, significant surface bubbling, and many cracks. The surface of W8, however, is covered by fine and uniform corrosion products, which is very dense with no cracks, thus protecting the substrate.

Figure 3 shows the microscopic morphologies of the experimental steels after the removal of the rust. The surfaces of W1–W4 exhibit many pitting pits and severe uniform corrosion morphology. W5–W7 present many localized corrosion features. There are virtually no obvious corrosion marks on the surface of W8, but a small number of small pits. These results show that, in the Cr content range from 1 to 4%, the uniform corrosion decreases and the local corrosion increases as the Cr content increases. In the Cr content range from 5 to 7%, the depth and the number of pitting pits decrease with increasing Cr content. When the Cr content reaches 8%, the corrosion behavior of the surface changes suddenly, resulting in improved corrosion resistance and less surface corrosion. These results are consistent with the other studies, which had a conclusion that the local corrosion of steel becomes more obvious, and the interface of the base rust layer becomes uneven after adding Cr to steel[33]. The scanning electron microscopic (SEM) observation results of the rust layer cross-section are shown in Fig. 4, and energy-dispersive spectroscopic (EDS) line scan analysis was performed on the marked areas in Fig. 4. It can be seen from the cross-sectional topography that there is no obvious delamination in the rust layer. For W1–W4, the number of the pitting pits increases gradually as the Cr content increases, the rust layer cross-section is uneven, and there are many microscopic cracks and holes. Samples W5–W7 exhibit significant local corrosion, the bonding between the rust layer and the substrate is weak, and large cracks exist in the rust layer. The rust layer of W8 is the thinnest, with a thickness only ~20 μm. The rust layer structure is very dense and exhibits good bonding with the matrix. It can be seen from the EDS line scan that the rust layer near the substrate is enriched in Cr. Cl^- exists in the entire rust layer and is slightly higher in the inner layer than that in the outer rust layer. This indicates that the rust layer is an ion conduction layer, and Cl^- can penetrate through the rust layer to the metal interface, causing corrosion reaction therewith; this gradually increases the density of the rust layer. Cracks and holes also appear in the cross-section of the rust layer. This is because the rust layer contains various corrosion products, and the densities of different corrosion products are different and smaller than that of the matrix. During the continuous accumulation of corrosion products on the surface of the steel substrate, stress is generated at the interface between the rust layer and the substrate, and corrosion products themselves have poor ductility, resulting in cracks and holes.

The X-ray diffraction (XRD) analysis on the rust layers of the samples after the wet–dry cycles corrosion test was performed, and the results are shown in Fig. 5. It can be seen from figure that, for all the samples analyzed, the rust layers contain α-FeOOH, γ-FeOOH, and Fe_3O_4. However, the content of each substance is significantly different in the different samples. Therefore, the *K* value method was used in order to semi-quantitatively analyze the rust layers to calculate the proportion of different phases in the rust layers. The results are shown in Table 1.

It can be seen from the table that, during the initial 24 h of corrosion, the rust layers of W1–W6 contain a large amount of Fe_3O_4, while those of W7 and W8 only contain α-FeOOH. At 72 and 120 h, surface corrosion of the samples became more extensive, and the proportion of Fe_3O_4 is detectably higher, which is consistent with the increase in the black rust amount, as evidenced by the macroscopic morphology results (Supplementary Fig. 1). After 168 h, the proportion of Fe_3O_4 becomes relatively small. Most of the corrosion products for W1–W7 are Fe_3O_4, while most of the corrosion products for W8 are α-FeOOH and γ-FeOOH with almost no Fe_3O_4. The proportion of α-FeOOH increases with the increase of number of corrosion cycles.

The XRD results show that increasing the Cr content has little effect on the γ-FeOOH content in the rust layer, which remains at a low level. Therefore, for each experimental steel we analyzed the relationship between the corrosion rate and the ratio of Fe_3O_4 in the rust layer for different corrosion cycles (Fig. 6). For each corrosion cycle, the ratio of Fe_3O_4 in the corrosion product of W8 is consistent with its corrosion rate. After 168 h, it can be seen clearly that the Fe_3O_4 ratio can be categorized into three groups based on the Cr content. For W1–W4, the ratio of Fe_3O_4 remains stable at ~92%. For W4–W7, the ratio of Fe_3O_4 decreases linearly from 92 to 73%, while the rust layer of W8 contains only 0.9% Fe_3O_4. This change of Fe_3O_4 content in the rust layer is consistent with the results from the corrosion rate change curve.

DISCUSSION

The polarization curves (Supplementary Fig. 3) of the eight experimental materials in the 3.5% NaCl solution shown that the corrosion resistance of the steel matrix improves as the Cr content increases. This is consistent with the traditional understanding of the role of Cr element but not with the results observed in the

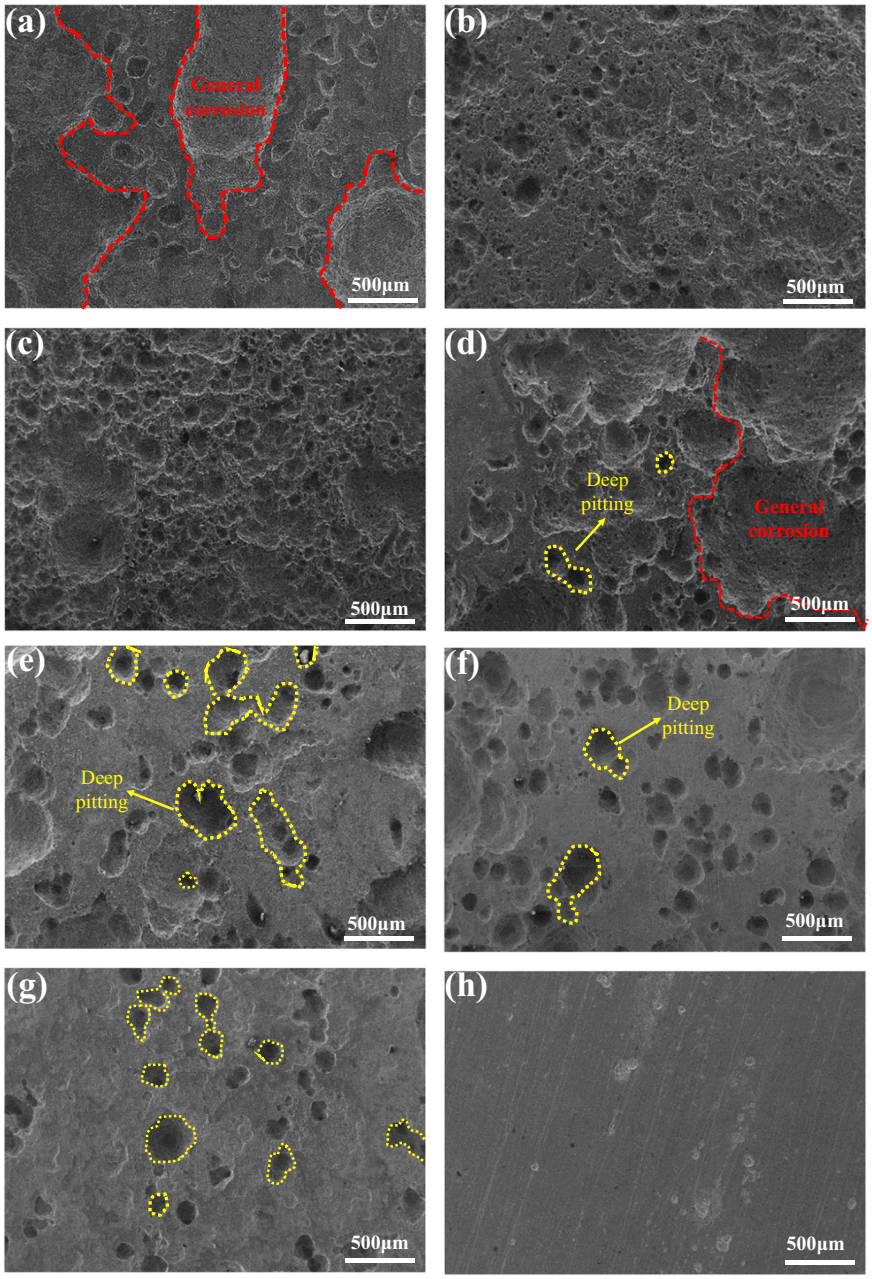

Fig. 3 Micro morphologies of eight experimental steels (rust removal) after 168 h alternating wet–dry cycles. a–h correspond to W1–W8 samples, respectively. The area marked with the red line is general corrosion area and marked by the yellow line is the severe pitting corrosion area. The surface corrosion form changes with Cr content. Localized corrosion of steel becomes more obvious from W2 to W7 samples.

atmospheric corrosion process. In order to further investigate this difference, the microscopic structure change of the substrate caused by Cr was studied to further clarify the reason for improving the corrosion resistance of the substrate. Many studies[34–36] investigated the possibility that the steel structure affects the corrosion resistance, and the addition of alloying elements changes the microstructure of the steel matrix, which in turn can affect its corrosion resistance. Our work showed that, when Cr was added as an alloying element to low-carbon steel, it delayed the pearlite transformation and promoted the bainite transformation, allowing the bainite structure to form more easily after austenitization. It can also be seen from Fig. 1 that the addition of Cr does changes the original phase structure of the material. When the Cr content is <4%, the material was composed of two phases of ferrite and bainite. When the Cr content was increased to 8%, the grain size further improved the corrosion resistance. Therefore, it is considered that the difference of the corrosion resistance in the experiment might be mainly contributed by the structural changes caused by the addition of different amount of Cr. To validate the hypothesis, W3 sample was selected for Kelvin probe force microscopy (KPFM) analysis. (Supplementary Fig. 4 and Fig. 7).

Supplementary Fig. 4 shows the metallographic structure of the W3 steel containing 3% Cr. The structure is composed of ferrite and granular bainite. The locus marked in the figure was where the KPFM testing performed. The KPFM result is shown in Fig. 7. Figure 7a–d are the height map, the potential map, the three-dimensional map of the potential, and the potential change curve

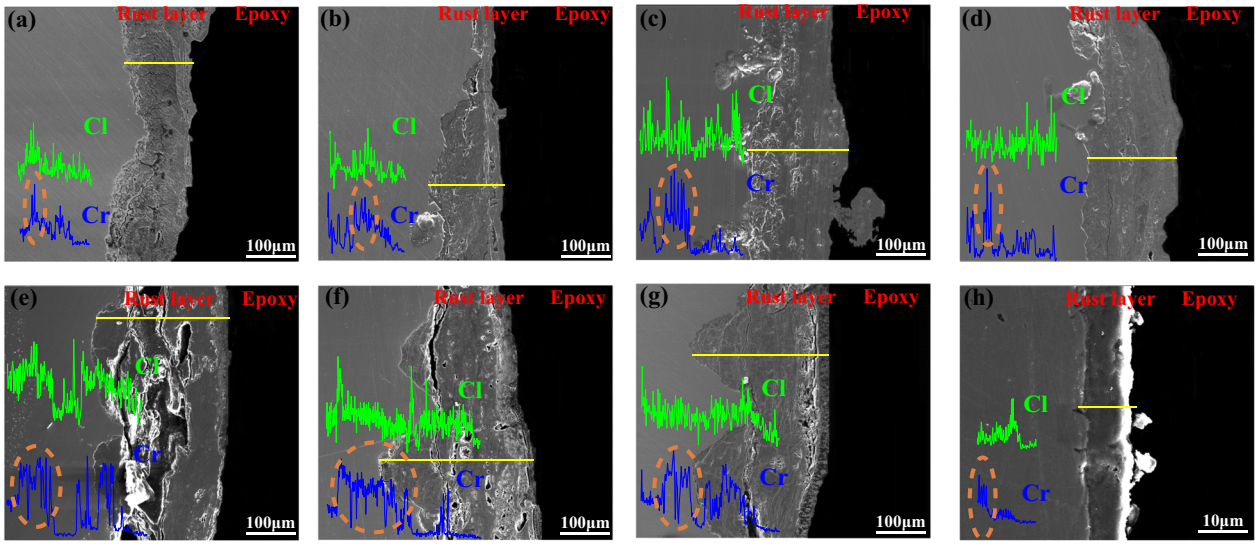

Fig. 4 Micro morphologies and Cl and Cr element line scan of the rust layers for eight experimental steels after wet–dry cycle corrosion for 168 h. a–h correspond to W1–W8 samples, respectively; the yellow line represents the EDS line scan position, the green curve for the Cl content variation, the blue curve for Cr content variation, the orange line marks the position of Cr enrichment.

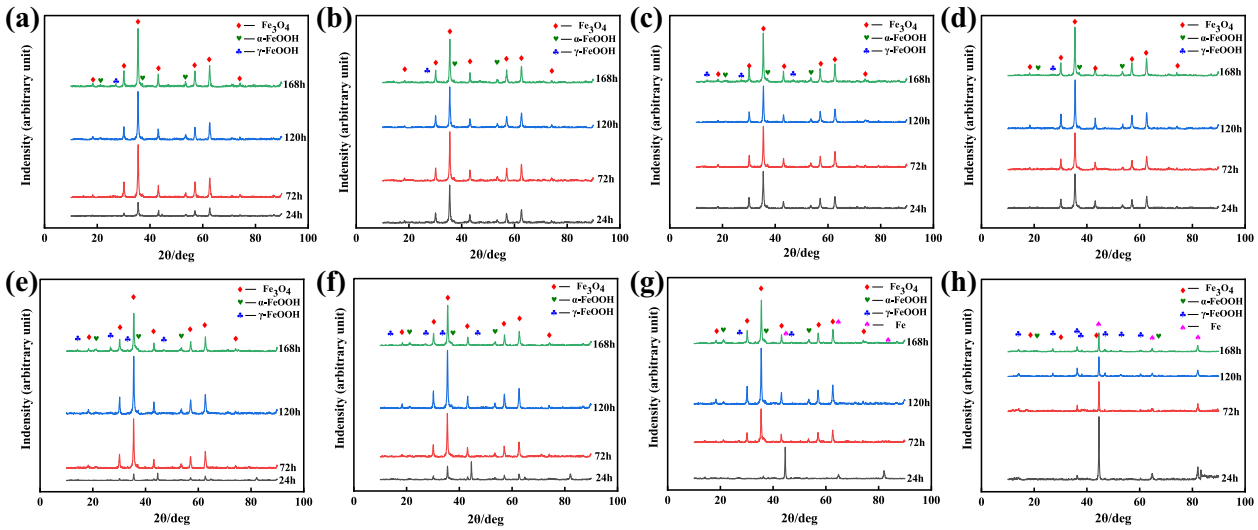

Fig. 5 X-ray diffraction diagrams of rust phases for eight experimental steels after wet–dry cycle corrosion for 24, 72, 120, and 168 h. a–h correspond to W1–W8 samples, respectively. The black, red, blue, and green lines represent for wet–dry cycle corrosion for 24, 72, 120, and 168 h, severally.

of the section, respectively. It can be seen from Fig. 7d that the potential of the granular bainite is much higher than the potential of the matrix ferrite, and the difference between the two is ~≥80 mV. The existence of this potential difference may have two effects. (1) The corrosion resistance of the steel matrix improves with more phase content that has better corrosion resistance, as shown in Fig. 2a and Supplementary Fig. 3 that display an early corrosion rate decrease. The corrosion resistance of the steel matrix continues to improve with the addition of more Cr content[29,37–39]. (2) The galvanic difference between the two phases caused the variations of the morphology and structure during the atmospheric corrosion process. Due to the difference of the potential between the two phases, the corrosion process is promoted and the corrosion morphology changes from uniform corrosion to local pitting, as shown in Fig. 3. At the later stage after a long-period dry–wet alternate corrosion process, the major factor that influence the corrosion rate became the structure of the rust layer. Therefore, a detailed analysis of the changes in the structure of the rust layer is also required.

The rust layer structure plays an important role in the corrosion resistance of materials[40,41]. In atmospheric corrosion, the main process on the material surface is the oxidation of Fe and the transformation of the rust layer. In Evans model[42], it is considered that a carbon steel undergoes strong cathodic depolarization in the rust layer at the beginning of corrosion and then an anodic reaction in the rust layer. This process occurs at the metal/Fe_3O_4 interface:

$$Fe \rightarrow Fe^{2+} + 2e^{-} \quad (1)$$

The cathodic reaction occurs at the Fe_3O_4/FeOOH interface:

$$Fe^{2+} + 8FeOOH + 2e \rightarrow 3Fe_3O_4 + 4H_2O \quad (2)$$

$$3Fe_3O_4 + 3/4O_2 + 9/2H_2O \rightarrow 9FeOOH \quad (3)$$

Table 1. Semi-quantitative analysis of rust layer XRD results.

Number	period	Fe_3O_4 (wt.%)	α-FeOOH (wt.%)	γ-FeOOH (wt.%)
W1	24 h	84.57157	15.42843	0
	72 h	94.97698	2.433409	2.589607
	120 h	94.46285	0	5.537148
	168 h	92.74633	2.08922	5.164446
W2	24 h	90.46199	6.302565	3.235448
	72 h	97.693	0	2.307004
	120 h	95.57277	0	4.427234
	168 h	92.2527	3.897821	3.849475
W3	24 h	89.17726	10.82274	0
	72 h	96.78247	0	3.217528
	120 h	96.3087	0	3.691301
	168 h	90.77812	4.26159	4.960292
W4	24 h	87.33965	6.457475	6.202879
	72 h	91.09919	2.112929′	6.787885
	120 h	96.28258	0	3.717421
	168 h	94.20305	2.495278	3.301669
W5	24 h	77.43117	22.56883	0
	72 h	95.23767	0	4.762329
	120 h	95.84923	0	4.150765
	168 h	83.20685	5.125722	11.66742
W6	24 h	76.53408	16.6905	6.775412
	72 h	94.01022	0	5.989777
	120 h	93.85057	0	6.149432
	168 h	76.78732	14.32297	8.889715
W7	24 h	0	100	0
	72 h	73.21516	15.47285	11.31199
	120 h	92.93271	0	7.067288
	168 h	73.77694	14.75088	11.47218
W8	24 h	0	100	0
	72 h	0	43.52924	56.47076
	120 h	0	88.43245	11.56755
	168 h	0.881889	91.302	7.816115

It is considered that α-FeOOH is an insulating inactive substance, which is the most stable hydroxy iron oxide and a main constituent of the protective rust layer. Tanaka et al.[43] identified that Fe_3O_4 plays an important role in reducing the corrosion resistance of rust layers, while α-FeOOH and γ-FeOOH promote the formation of Fe_3O_4. Fe_3O_4 serves as a conductor in the rust layer. Its conductivity is similar to that of pure metal. The electrons in the metal can be transferred by Fe_3O_4 as carriers. Therefore, when the rust layer contains a large amount of Fe_3O_4, it does not provide a protective effect. Instead, Fe_3O_4 acts as an active point on the surface and provides carriers for the electrochemical process, thus promoting the corrosion process of metals. Addition of Cr can have two effects on the alteration of low-carbon steel rust layer. On the one hand, Cr often exists in the form of Cr^{3+}, which replaces Fe^{3+} ions in FeOOH[44]. This breaks the balance process in Eq. (3) above, thus accelerating the conversion of Fe_3O_4 into FeOOH and promoting the formation of FeOOH (Fig. 5 and Table 1). To validate this, the content of the rust layers of the samples after 168 h of the wet–dry cycles corrosion is plotted in Fig. 8 along with their Cr content. The figure shows that, as Cr content increases, the content of Fe_3O_4 decreases continuously, while FeOOH increases. On the other hand, as a general passivation element, the addition of Cr will inevitably increase the passivation tendency of the material's surface, thereby suppressing the reaction process. In summary, Cr addition affects the passivation and rust layer structure of steels, thereby suppressing the corrosion process.

In the present work, the effect of Cr addition on the corrosion resistance of low-corrosion-resistance steels was investigated using KPFM and dry–wet cycle corrosion testing. The following conclusions were drawn from the present study:

- The corrosion resistance for the long-period atmospheric corrosion can be significantly improved when the Cr content is >4%. For the low-carbon steel with 1–8% Cr content, the effect of Cr content on the atmospheric corrosion rate can be divided into three ranges: almost no effect <4%, a negative correlation at 4–7%, and a step point at 8% content.
- When the Cr content is <4%, it has almost no effect on the Fe_3O_4 content in the atmospheric corrosion rust layer. When the Cr content is >4%, the Cr content can promote the conversion of Fe_3O_4 to FeOOH in the rust layer, and this conversion and Cr content present positive correlation.

METHODS

Materials preparation

Eight groups of experimental steel samples with different Cr contents marked as W1, W2, W3, W4, W5, W6, W7, and W8 were prepared. The compositions of these samples are shown in Table 2. They were prepared by vacuum melting and then casting into round ingots, followed by 1-h homogenization at 1200 °C. The steel ingots were rolled into 6-mm-thick strips with a final rolling temperature of approximately 900 °C, followed by water quenching to 520–540 °C and then air cooled to room temperature. In order to eliminate internal stress from the rolling process, the samples were normalized at 850 °C for 0.5 h. The detailed process is described in Supplementary Fig. 5. The final samples were cut into 10 mm × 10 mm × 3 mm. All the samples were sanded to 2000#, polished, and etched with 4% nitric acid alcohol solution to observe the microstructure.

Wet–dry cyclic corrosion test

The dry–wet cycle experiment is generally considered as one of the more efficient methods for simulating atmospheric corrosion because of its similarity with the actual outdoor corrosion[45,46]. Each cycle of the wet/dry corrosion test is 1 h, which consists of two stages: (1) immersing the specimens in a 0.5% NaCl solution with pH = 3.0 at 40 °C for 45 min and (2) drying the specimens with four heating lamps for 15 min. The relative humidity inside the testing container was maintained at 70% (±5%) during the experiment. The samples have a size of 50 mm × 25 mm × 3 mm, and each experimental group was made of three samples. Prior to the experiments, all of the samples were processed as follows: sanding (to 1500#) → pure water cleaning → acetone degreasing → anhydrous ethanol dehydration → 24-h drying. The experimental periods were 24, 72, 120, and 168 h. For each sample, the initial weight was recorded as W_0 (accurate to 0.0001 g), and the sample size was measured using a Vernier caliper. After the experiment, all the samples were placed in an ultrasonic cleaner with a solution of 500 mL HCl + 500 mL H_2O + 3.5 g hexamethylenetetramine at 25 °C for about 15 min to remove the corrosion product[47]. Then the samples were rinsed using deionized water, followed by anhydrous alcohol and dried in cold air. The final masses W_t were recorded (accurate to 0.0001 g). Meanwhile, an untreated sample also went through the same processes for each steel to calibrate the mass loss produced during the process of removing corrosion products. The corrosion rates (R, mm y^{-1}) were calculated as follows:

$$R = 8.76 \times 10^4 \frac{W_0 - W_t}{S\rho t}, \quad (4)$$

where $(W_0 - W_t)$ represents the weight loss of the sample after the dry–wet cyclic corrosion test, measured in grams; S represents the exposed area of the sample and is in cm^2; ρ represents the sample's density and was taken as 7.8 g cm^{-3}; and t is the test time in years.

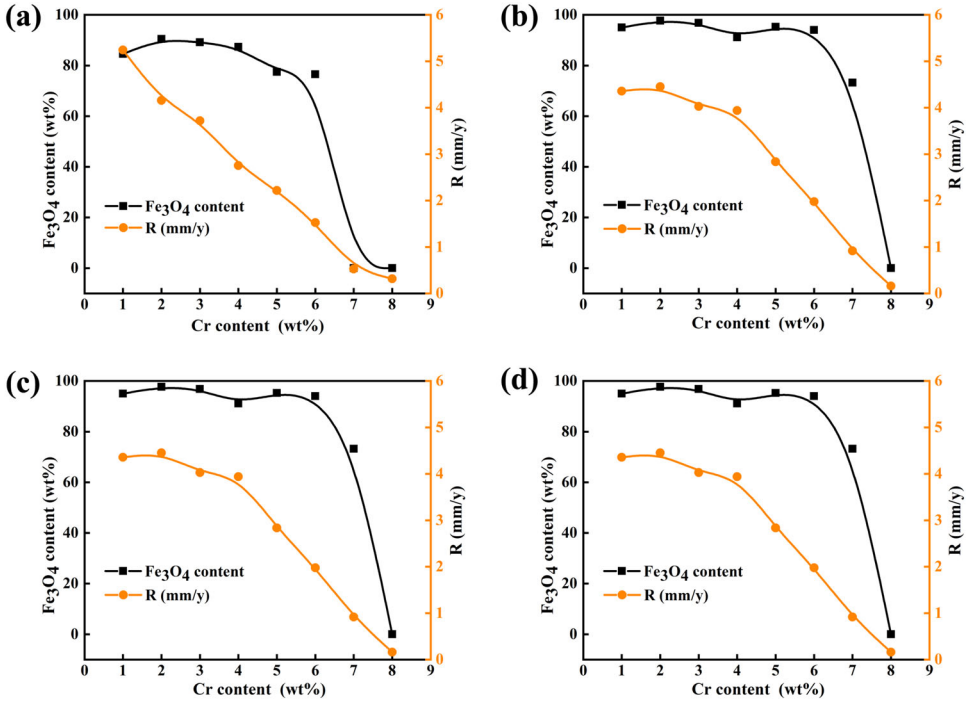

Fig. 6 Variation tendency of Fe_3O_4 content in corrosion products and corrosion rate for eight experimental steels during various wet–dry corrosion cycles. a 24 h, **b** 72 h, **c** 120 h, **d** 168 h. The orange lines in **a**–**d** all represent the change curve of corrosion rate, and the black line represents the change of Fe_3O_4 content of corrosion products.

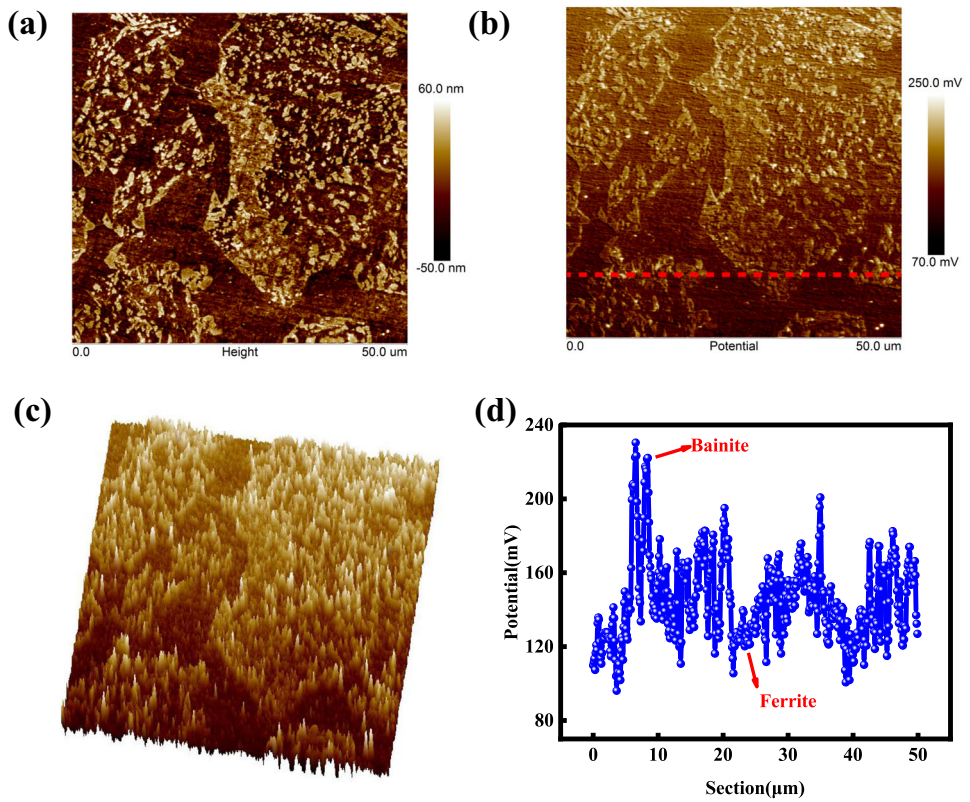

Fig. 7 The KPFM of different structure in 3% Cr content experimental steel. a Height map, **b** Potential map, **c** 3D map of potential, **d** potential change curve of the red section line in **b**.

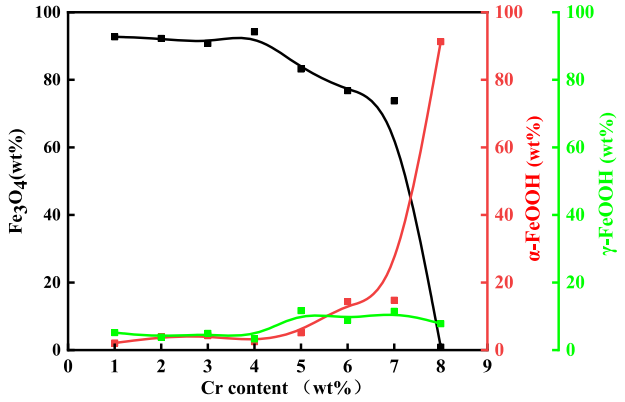

Fig. 8 The content of constituents in rust layer as a function of Cr content after 168 h alternating wet–dry cycles. The black, red, and green lines correspond to the variation of Fe_3O_4, α-FeOOH, and γ-FeOOH versus Cr content.

Table 2. Chemical composition of the experiment materials.

Materials	Element compositions (wt.%)					
	C	Si	Mn	P	S	Cr
W1	0.037	0.035	1.06	0.008	0.0072	1.02
W2	0.035	0.045	1.12	0.009	0.0080	1.94
W3	0.037	0.058	1.22	0.008	0.0080	3.06
W4	0.043	0.042	1.12	0.008	0.0075	3.98
W5	0.052	0.044	1.15	0.008	0.0075	5.09
W6	0.054	0.057	1.13	0.009	0.0070	6.09
W7	0.054	0.053	1.14	0.008	0.0083	7.07
W8	0.058	0.045	1.09	0.008	0.0082	7.78

Corrosion morphology and rust analysis

Surface and cross-sectional morphologies of the samples were observed using a KEYENCE VX-200 stereomicroscope and a FEI Quanta250 SEM. Their rust layers were analyzed with an EDS. The phases in the corrosion products were determined by XRD on a Rigaku analyzer over a 10–90° range with a scanning rate of 4 ° min^{-1}. The parameters of the generator were set to 40 kV and 40 mA.

Electrochemical test

Electrochemical tests were performed using a M2273 electrochemical workstation and a three-electrode system, where the samples were used as the working electrodes, a Pt plate as the counter electrode, and a saturated calomel electrode (SCE) as the reference electrode. The test solution was 0.5% NaCl (pH = 3). The samples were cut to 10 mm × 10 mm × 3 mm in size and were then covered with epoxy resin with a 1.0-cm^2 exposed area. Prior to each test, the open circuit potential (OCP) was monitored for at least 20 min until it reached a stable state. Potentiodynamic polarization tests ranged from −0.25 V (versus OCP) to −0.3 V_{SCE}, and the scanning rate was 0.5 mV s^{-1}. All of the measurements were performed at room temperature (~25 °C) and were repeated three times to ensure reproducibility.

KPFM test

Atomic force microscope (Multimode 8, Bruker) is used in the KPFM measurements. The equipment was located in a clean room at a constant temperature of 25 °C and an ambient relative humidity of approximately 20%. The probes used in the KPFM measurements were PFQNE-AL with a force constant of 1.5 N m^{-1} and a resonant frequency of 300 kHz. The dual-scan mode was used to record the second signal in addition to the surface topographic signal. In a KPFM measurement, when a potential difference exists between the tip and the sample, an AC voltage is applied to the tip to induce harmonic oscillation of the cantilever. Afterwards, a voltage of the same magnitude is applied to the tip to stop the oscillation and reduce the potential difference. Using this method, the work function of the sample can be derived. Some studies have shown that the work function is closely related to the corrosion potential. The lower the work function of a material, the lower the corrosion potential and the easier the corrosion[48,49].

DATA AVAILABILITY

The data of this study are available from the corresponding authors upon reasonable request.

Received: 15 June 2020; Accepted: 19 October 2020;
Published online: 17 November 2020

REFERENCES

1. Cui, Z. et al. Passivation behavior and surface chemistry of 2507 super duplex stainless steel in artificial seawater: influence of dissolved oxygen and pH. *Corros. Sci.* **150**, 218–234 (2019).
2. Yao, J., Macdonald, D. D. & Dong, C. Passive film on 2205 duplex stainless steel studied by photo-electrochemistry and ARXPS methods. *Corros. Sci.* **146**, 221–232 (2019).
3. Liu, M., Cheng, X., Li, X., Pan, Y. & Li, J. Effect of Cr on the passive film formation mechanism of steel rebar in saturated calcium hydroxide solution. *Appl. Surf. Sci.* **389**, 1182–1191 (2016).
4. Tewary, N. K., Kundu, A., Nandi, R., Saha, J. & Ghosh, S. Microstructural characterisation and corrosion performance of old railway girder bridge steel and modern weathering structural steel. *Corros. Sci.* **113**, 57–63 (2016).
5. Hao, L., Zhang, S., Dong, J. & Ke, W. Atmospheric corrosion resistance of MnCuP weathering steel in simulated environments. *Corros. Sci.* **53**, 4187–4192 (2011).
6. Cheng, X., Jin, Z., Liu, M. & Li, X. Optimizing the nickel content in weathering steels to enhance their corrosion resistance in acidic atmospheres. *Corros. Sci.* **115**, 135–142 (2017).
7. Thee, C. et al. Atmospheric corrosion monitoring of a weathering steel under an electrolyte film in cyclic wet-dry condition. *Corros. Sci.* **78**, 130–137 (2014).
8. Morcillo, M., Chico, B., Díaz, I., Cano, H. & De la Fuente, D. Atmospheric corrosion data of weathering steels. A review. *Corros. Sci.* **77**, 6–24 (2013).
9. Li, X. et al. Share corrosion data. *Nature* **527**, 441–442 (2015).
10. Fu, G., Zhu, M. & Gao, X. Rust layer formed on low carbon weathering steels with different Mn, Ni contents in environment containing chloride ions. *Mater. Sci.* **22**, 501–505 (2016).
11. Zhou, Y., Chen, J., Xu, Y. & Liu, Z. Effects of Cr, Ni and Cu on the corrosion behavior of low carbon microalloying steel in a CF-containing environment. *J. Mater. Sci. Technol.* **29**, 168–174 (2013).
12. Cheng, X., Tian, Y., Li, X. & Zhou, C. Corrosion behavior of nickel-containing weathering steel in simulated marine atmospheric environment. *Mater. Corros.* **65**, 1033–1037 (2014).
13. Wu, W., Cheng, X., Hou, H., Liu, B. & Li, X. Insight into the product film formed on Ni-advanced weathering steel in a tropical marine atmosphere. *Appl. Surf. Sci.* **436**, 80–89 (2018).
14. Morcillo, M., Díaz, I., Cano, H., Chico, B. & De, lF. D. Atmospheric corrosion of weathering steels. Overview for engineers. Part I: Basic concepts. *Constr. Build. Mater.* **213**, 723–737 (2019).
15. Cano, H. et al. Characterization of corrosion products formed on Ni 2.4wt%-Cu 0.5wt%-Cr 0.5wt% weathering steel exposed in marine atmospheres. *Corros. Sci.* **87**, 438–451 (2014).
16. Ma, Y., Li, Y. & Wang, F. Weatherability of 09CuPCrNi steel in a tropical marine environment. *Corros. Sci.* **51**, 1725–1732 (2009).
17. Song, L., Chen, Z. & Hou, B. The role of the photovoltaic effect of γ-FeOOH and β-FeOOH on the corrosion of 09CuPCrNi weathering steel under visible light. *Corros. Sci.* **93**, 191–200 (2015).
18. Yamashita, M., Miyuki, H., Matsuda, Y., Nagano, H. & Misawa, T. The long term growth of the protective rust layer formed on weathering steel by atmospheric corrosion during a quarter of a century. *Corros. Sci.* **36**, 283–299 (1994).
19. Díaz, I. et al. Five-year atmospheric corrosion of Cu, Cr and Ni weathering steels in a wide range of environments. *Corros. Sci.* **141**, 146–157 (2018).
20. Kamimura, T., Hara, S., Miyuki, H., Yamashita, M. & Uchida, H. Composition and protective ability of rust layer formed on weathering steel exposed to various environments. *Corros. Sci.* **48**, 2799–2812 (2006).
21. Kamimura, T. & Stratmann, M. The influence of chromium on the atmospheric corrosion of steel. *Corros. Sci.* **43**, 429–447 (2001).

22. Larrabee, C.P. & Coburn, S. k. The atmospheric corrosion of steels as influenced by changes in chemical composition, Proc. 1st International Congress on Metallic Corrosion, London, 279–285 (1961).
23. Nishimura, T., Katayama, H., Noda, K. & Kodama, T. Effect of Co and Ni on the corrosion behavior of low alloy steels in wet/dry environments. *Corros. Sci.* **42**, 1611–1621 (2000).
24. Wang, B., Xu, L., Zhu, J., Xiao, H. & Lu, M. Observation and analysis of pseudo-passive film on 6.5%Cr steel in CO_2 corrosion environment. *Corros. Sci.* **111**, 711–719 (2016).
25. Zhu, J. et al. Essential criterion for evaluating the corrosion resistance of 3Cr steel in CO_2 environments: prepassivation. *Corros. Sci.* **93**, 336–340 (2015).
26. Jiang, S., Chai, F., Su, H. & Yang, C. Influence of chromium on the flow-accelerated corrosion behavior of low alloy steels in 3.5% NaCl solution. *Corros. Sci.* **123**, 217–227 (2017).
27. Yamashita, M., Shimizu, T., Konishi, H., Mizuki, J. & Uchida, H. Structure and protective performance of atmospheric corrosion product of Fe-Cr alloy film analyzed by Mssbauer spectroscopy and with synchrotron radiation X-rays. *Corros. Sci.* **45**, 381–394 (2003).
28. Qian, Y., Ma, C., Niu, D., Xu, J. & Li, M. Influence of alloyed chromium on the atmospheric corrosion resistance of weathering steels. *Corros. Sci.* **74**, 424–429 (2013).
29. Qian, Y., Niu, D., Xu, J. & Li, M. The influence of chromium content on the electrochemical behavior of weathering steels. *Corros. Sci.* **71**, 72–77 (2013).
30. Guo, S., Xu, L., Zhang, L., Chang, W. & Lu, M. Corrosion of alloy steels containing 2% chromium in CO_2 environments. *Corros. Sci.* **63**, 246–258 (2012).
31. Morcillo, M., Diaz, I., Chico, B., Cano, H. & Fuente, D. D. L. Weathering steels: from empirical development to scientific design. A review. *Corros. Sci.* **83**, 6–31 (2014).
32. Xu, L., Wang, B., Zhu, J., Li, W. & Zheng, Z. Effect of Cr content on the corrosion performance of low-Cr alloy steel in a CO_2 environment. *Appl. Surf. Sci.* **379**, 39–46 (2016).
33. Tahara, A. & Shinohara, T. Influence of the alloy element on corrosion morphology of the low alloy steels exposed to the atmospheric environments. *Corros. Sci.* **47**, 2589–2598 (2005).
34. Wang, C., Wang, T., Cao, L. & Zhang, G. The effect of phase structure on the corrosion behavior of Al100-xMox alloy thin films. *J. Alloy. Compd.* **790**, 563–571 (2019).
35. Cano, H. Atmospheric corrosion of weathering steels. Overview for engineers. Part II: Testing, inspection, maintenance. *Constr. Build. Mater.* **222**, 750–765 (2019).
36. Gong, W. et al. Effects of ausforming temperature on bainite transformation, microstructure and variant selection in nanobainite steel. *Acta Mater.* **61**, 4142–4154 (2013).
37. Uhlig, H. H. & King, C. Corrosion and corrosion control. *J. Electrochem. Soc.* **119**, 327C (1972).
38. Ha, H. Y., Lee, T. H., Lee, C. G. & Yoon, H. Understanding the relation between pitting corrosion resistance and phase fraction of S32101 duplex stainless steel. *Corros. Sci.* **149**, 226–235 (2019).
39. Zhang, Y., Huang, F., Hu, Q., Peng, Z. & Liu, J. Effect of micro-phase electrochemical activity on the initial corrosion dynamics of weathering steel. *Mater. Chem. Phys.* **241**, 122045 (2020).
40. Tamura, H. The role of rusts in corrosion and corrosion protection of iron and steel. *Corros. Sci.* **50**, 1872–1883 (2008).
41. Rocca, E., Faiz, H., Dillmann, P., Neff, D. & Mirambet, F. Electrochemical behavior of thick rust layers on steel artefact: mechanism of corrosion inhibition. *Electrochim. Acta* **316**, 219–227 (2019).
42. Evans, U. R. & Taylor, C. A. J. Mechanism of atmospheric rusting. *Corros. Sci.* **12**, 227–246 (1972).
43. Tanaka, H., Mishima, R., Hatanaka, N., Ishikawa, T. & Nakayama, T. Formation of magnetite rust particles by reacting iron powder with artificial α-, β- and γ-FeOOH in aqueous media. *Corros. Sci.* **78**, 384–387 (2014).
44. Mancio, M., Kusinski, G., Monteiro, P. J. M. & Devine, T. M. Electrochemical and in-situ SERS study of passive film characteristics and corrosion performance of 9%Cr microcomposite steel in highly alkaline environments. *J. ASTM Int.* **6**, 1–10 (2009).
45. Lyon, S. B., Thompson, G. E. & Johnson, J. B. Accelerated atmospheric corrosion testing using a cyclic wet/dry exposure test: aluminum, galvanized steel, and steel. *Corrosion* **43**, 719–726 (1987).
46. Zhu, F., Persson, D. & Thierry, D. Formation of corrosion products on open and confined metal surfaces exposed to periodic wet/dry conditions-a comparison between zinc and electrogalvanized steel. *Corrosion* **57**, 582–590 (2001).
47. British Standards Institute Staff. *ISO 8407. Corrosion of Metals and Alloys. Removal of Corrosion Products from Corrosion Test Specimens* (B S I Standards, 2009).
48. Lacroix, L., Laurence, R., Christine, B. & Georges, M. Combination of AFM, SKPFM, and SIMS to study the corrosion behavior of S-phase particles in AA2024-T351. *J. Electrochem. Soc.* **155**, C131 (2008).
49. Li, M., Guo, L. Q., Qiao, L. J. & Bai, Y. The mechanism of hydrogen-induced pitting corrosion in duplex stainless steel studied by SKPFM. *Corros. Sci.* **60**, 76–81 (2012).

ACKNOWLEDGEMENTS

The authors acknowledge the support of the National Natural Science Foundation of China (No. 51671028) and the National Key Research and Development Program of China (No. 2016YFB0300604)

AUTHOR CONTRIBUTIONS

X.C. and X.Z. conceived the project and designed the experiments. B.S. and X.Z. performed the experiments and analyses. B.S. wrote the paper. X.L. and X.C. revised the paper. All the authors contributed to the interpretation of the experimental data and discussed the results.

COMPETING INTERESTS

The authors declare no competing interests.

ADDITIONAL INFORMATION

Supplementary information is available for this paper at https://doi.org/10.1038/s41529-020-00142-5.

Correspondence and requests for materials should be addressed to X.C. or X.L.

Reprints and permission information is available at http://www.nature.com/reprints

Publisher's note Springer Nature remains neutral with regard to jurisdictional claims in published maps and institutional affiliations.